A coupled Thermal-mechanical FE Model of Flow Localization during the Hot Torsion Test

Bahman MIRZAKHANI[1], Shahin KHODDAM[2], Hossein ARABI[1], Mohammad Taghi SALEHI[1], Jilt SIETSMA[3]

[1] Department of Materials and Metallurgical Engineering, Iran University of Science and Technology, P.O. Box 16844-13114, Tehran, Iran
[2] Mechanical Engineering Department, Monash University, Clayton Campus, Vic 3800, Australia
[2] Department of Materials Science and Engineering, Delft University of Technology, Mekelweg 2, 2628 CD Delft, the Netherlands

The hot torsion test (HTT) has been extensively used to analyse and physically model the flow behaviour and microstructure evolution of materials and alloys during hot deformation processes. The geometry of the specimen is a key factor for obtaining reliable results. In the present work, a thermo-rigid viscoplastic FE code, THORAX.FOR, was developed to describe the interaction of thermal-mechanical conditions and geometries of the HTT specimens. This was used to recommend the conditions for avoiding flow localization during HTT of API-X70 microalloyed steel. The simulation results show how an inappropriate choice of both test specimen geometry and twist rate of deformation could lead to a significant temperature raise in the middle of the gauge section and temperature gradient in the radial and longitudinal direction of the specimen. This consequently causes flow localization during the test. Therefore, assumptions of isothermal forming conditions or uniform strain softening may not be valid in many test scenarios. These assumptions could introduce significant errors in the post results of the test such as flow curve and interpretation of microstructure evolution. Recommendations on proper specimen geometry for a specified strain rate will be given to avoid flow localization during the hot torsion test.

Introduction

The hot torsion test (HTT) has been one of the most popular mechanical tests for assessment of workability of metals and alloys for bulk forming processes during the last decades [1-6]. The simple feature of the torsion test is that a constant true strain and true strain rate can be imposed by simply twisting one end relative to the other at a constant angular velocity. In this test, the specimens do not undergo a significant shape change during deformation as long as the gauge section is restrained to a fixed length. It is often chosen over the uniaxial tension and compression tests because very large strains and strain rates can be achieved without the problems of necking and barrelling [7].

However, to overcome the test rig limitations and to obtain the required strain and strain rate range, a wide range of specimen geometries and sizes have been used [1-6]. Failure to justify these choices may lead to some serious errors in deriving the constitutive parameters for a given material, due to the non-uniform temperature and localization of stress and deformation within the gauge section of the test samples. These errors have not been investigated systematically.

Rebelo and Kobayashi [8] used the finite element formulations for a coupled analysis of deformation and heat transfer, to simulate temperature distributions during hot compression of an aluminium solid cylinder and a ring. Moal et al. [9] used a power law constitutive equation in a thermo-mechanical model of a nickel-base alloy for prediction of self-heating during a high speed torsion test for only a short sample of 6mm length. They showed that the maximum values of the torque obtained from simulation results were in good agreement with the experimental data. Their thermal analysis did not include

radiation effects. Khoddam et al. [10] showed for some HTT specimen geometries that deformation of the shoulders introduces errors to the determination of the constitutive parameters by rigid viscoplastic FE simulation. They also developed an analytical iterative technique for determination of the effective length, which takes into account the deformation outside the gauge section of a hot torsion test specimen assuming an isothermal deformation [11]. Zhou and Clode [12] used a heat conduction FE model to predict the temperature rise during hot torsion testing of an AA5252 aluminium alloy but they assumed a constant temperature within the gauge section of the HTT specimens. Njiwa et al. [13] presented a numerical approach for determining the effect of self heating on the shape of the torque-twist curve for a fixed geometry of the HTT sample. They did not take into account the influence of the specimen geometry and the twisting rate on temperature distribution.

In the present work, a coupled thermal-mechanical FE model has been described and used to investigate the effects of specimen geometry and process conditions on the distribution of thermomechanical parameters within the specimen during hot torsion testing. This will help to prevent flow localization by finding optimum specimen geometry and deformation conditions. Consequently, this minimizes the negative impact of flow localization by determining the reliable flow curve data form the HTT.

The present model, based on a flexible hot torsion test machine, has been developed at IROST [14].

Integrated Thermal-Mechanical Rigid-Viscoplastic Model for HTT

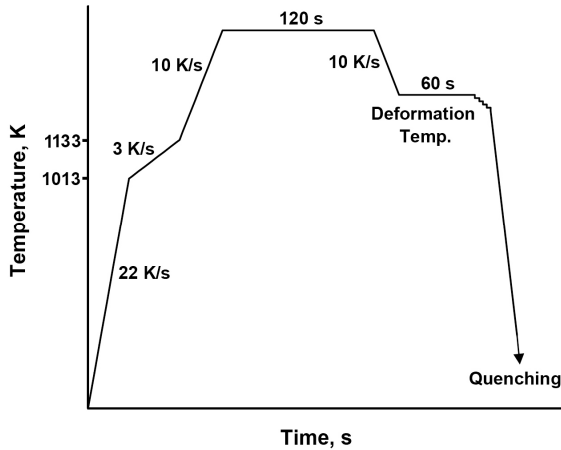**Reheating treatment.** Before starting the hot deformation, the material is heated up to a given

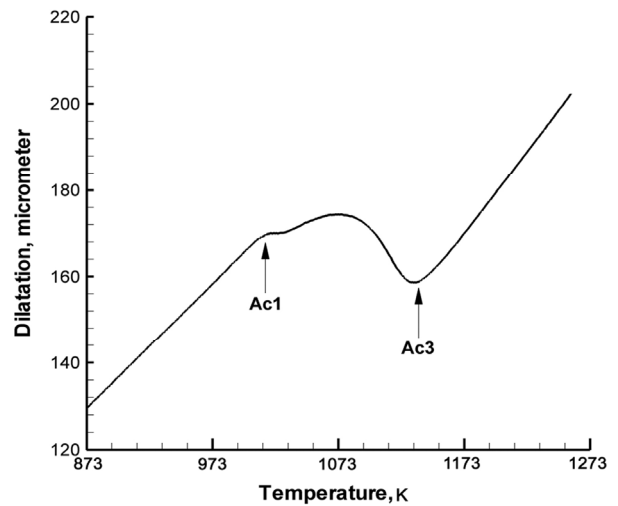**Figure 1.** Reheating cycle before hot torsion test.

Figure 2. Dilatation as a function of temperature in dilatometry test.
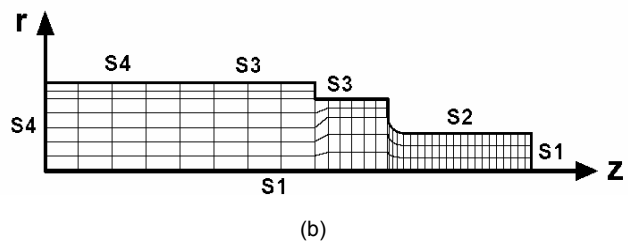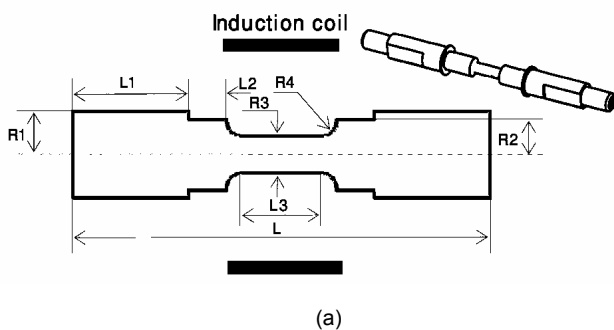

(a)

(b)

Figure 3. (a) Schematic of the geometry of a solid hot torsion specimen. (b) The domain and boundaries and mesh used for the FE modelling of the reheating treatment.

Table 1. Chemical position of the API-X70 steel used for the experiment, in mass%

C	Mn	Si	P	S	Nb	V	Ti	N	Fe
0.09	1.63	0.32	0.009	0.003	0.04	0.05	0.01	0.002	Bal.

temperature, soaked for a while and then cooled to the deformation temperature. During the hot torsion test, the heating energy is usually supplied by an induction or resistance type furnace [1-3,12-14]. In this study, reheating treatment was modelled using an FE code. A reheating cycle was designed for a micro-alloyed X70 steel as shown in **Figure 1**. The temperatures 1013 and 1133 K in this figure are Ac1 and Ac3 of the present microalloyed steel. They were determined by dilatometry tests as presented in **Figure 2**. In this range a rather low heating rate was considered in order to give time for ferrite and pearlite transformation to austenite. The chemical composition of the API-X70 microalloyed steel used in this study is given in **Table 1**.

The geometry of the HTT specimen used in this investigation is shown in **Figure 3a**. A two-dimensional FE analysis of heat flow has been used here to study the effect of the initial reheating cycle before deformation starts. The specimen dimensions are shown parametrically in order to consider the effect of each dimension. The domain, boundaries and the mesh which were used in the FE analysis to model the reheating treatment is also presented in **Figure 3b** where only one-quarter of a

longitudinal section of Figure 3a is considered because of the symmetry of geometry.

The axisymmetric condition during reheating treatment implies that heat flux along the boundaries S1 is zero or insulated. The boundary S2 is directly heated by an induction coil of 45 mm length. The heating was controlled by a pyrometer carefully located above the centre of the specimen. The boundary S3 is exposed to the surrounding environment where the energy loss is considered through both boundary convection and radiation. Radiation is between the specimen outer surface and the surface of a tubular enclosure placed between the induction coil and the specimen, to ensure a protecting atmosphere around the specimen. A simplified approach for radiation heat transfer was utilized by using an equivalent convection boundary condition, in which the non-linearity is considered through a temperature-dependent convection coefficient, which will be designated here as h_r:

$$h_r = \breve{\sigma}\varepsilon F_{s-te}\left[\left(T_s^2 + T_{te}^2\right)\left(T_s + T_{te}\right)\right]_{n-1} \tag{1}$$

where h_r is a temperature-dependent convection coefficient between two surfaces s and te, denoting the
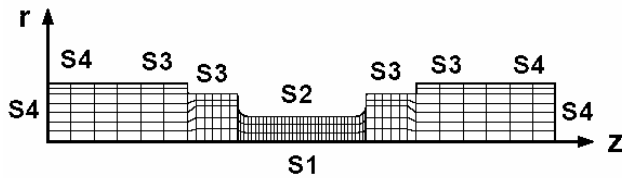
Figure 4. Domain and mesh used for the FE analysis of the hot torsion problem.

specimen and tubular enclosure surfaces respectively, at time step n. T_s and T_{te} are the absolute temperatures of these surfaces in Kelvin, $\breve{\sigma}$ is the Stefan-Boltzman coefficient and ε is the emissivity factor for the specimen surface. $F_{s\text{-}te}$ is the radiative shape factor between the two surfaces. The value of $\varepsilon = 0.65$ was adapted according to the ASTM standard test [15]. The radiative shape factor was calculated by a numerical integration scheme [11].

The boundary S4 is in contact with the grippers of the HTT machine. For these boundaries, the thermal contact conductance (k_{int}) of the interface between the specimen and the grips was considered and heat exchange modelled by convection.

The heat transfer characteristics of the steel used in the present work were assumed to be as follows [11 and 16]:

$\rho = 7800 \text{ kg·m}^{-3}$
$c = 680 \text{ J·kg·K}^{-1}$
$k = 36.8 \text{ W·m}^{-1}\text{·K}^{-1}$
$k_{int} = 3740 \text{ W·m}^{-2}\text{·K}^{-1}$
$T_g = 483 \text{ K}$
$T_a = 368 \text{ K}$
$\breve{\sigma} = 5.67 \cdot 10^{-8} \text{ W·m}^{-2}\text{·K}^{-4}$
$h = 4 \text{ W·m}^{-2}\text{·K}^{-1}$

where ρ and c are the density and heat capacity of the material respectively. The convective heat transfer coefficient and thermal conductivity are denoted by h and k, respectively. The subscript a refers to ambient and g to grip.

An integrated thermal-mechanical rigid-viscoplastic model for the HTT. Comparison of the predicted temperature distributions in a solid compression cylinder with experimental data, obtained by Rebelo and Kobayashi [8], showed the capabilities of the coupled thermo-viscoplastic analysis of non-steady-state metal forming processes. A rigid-viscoplastic FE formulation based on the principle of virtual work was utilized to calculate strain, strain rate and stress. According to this approach, for a volume V of the continuum and its boundary S, among admissible velocities u_i that satisfy the conditions of compatibility, incompressibility and boundary conditions, the actual solution gives the following functional (π) a stationary value [17, 18]:

$$\pi = \int_V \bar{\sigma} \dot{\bar{\varepsilon}} dV - \int_{S_F} F_i u_i dS \qquad (2)$$

where $\bar{\sigma}$ and $\dot{\bar{\varepsilon}}$ are effective stress and effective strain rate respectively and F_i represents surface tractions. The solution of the original boundary-value problem was obtained from the solution of the variational problem and the incompressibility constraint on admissible velocity

fields in Eq.(2) was removed by using a penalty constant. The procedure for discretizing the volume V, using iso-parametric quadrilateral elements, linearization of the stiffness equations and finally the iterative solution of the linearized equations can be found elsewhere [17]. These factors allow calculating the velocity field.

For an accurate analysis of the hot torsion test, the solution of plastic deformation and the thermal problem was coupled in the current model. The approach was based on the energy balance during a heat transfer for a given time as follows:

$$\frac{\partial q_x}{\partial x} + \frac{\partial q_y}{\partial y} + \frac{\partial q_z}{\partial z} + Q - \rho c \frac{\partial T}{\partial t} = 0 \qquad (3)$$

where q_x, q_y and q_z are components of the heat flow rate vector per unit area in Cartesian coordinates (x, y, z), t, T and Q are time, temperature and the heat generated due to plastic work respectively. The amount of Q can be estimated as:

$$Q = \kappa \sigma_{ij} \varepsilon_{ij} \qquad (4)$$

where κ is the heat generation efficiency and is assumed to be 0.9 in this work [17]. In fact, this term has an important role in raising the temperature of the sample during the deformation process especially at high deformation rates.

The elemental equations of the thermal problem were derived by the method of weighted residuals using Galerkin's criterion [18]. The detailed description of the thermal-mechanical rigid-viscoplastic model has been presented in [11].

Both thermal and mechanical analyses were performed using the same mesh. **Figure 4** shows the schematic of the 2D domain and the FE mesh used for the coupled thermal-mechanical analysis of a hot torsion specimen. The analyses were performed using at least 400 iso-parametric quadrilateral elements. In order to account for flow localization while minimizing the number of elements, different element sizes were used. In the gauge section and its neighbouring zones (fillets), the aspect ratio of the elements is near to one.

The boundary conditions consist of prescribed velocities at both ends of the specimen. The right shoulder is considered to be fixed while the left shoulder is twisted with a known angular velocity. The boundary conditions of the heat transfer problem during the hot torsion test are similar to the reheating problem, as discussed before. The initial temperature is also obtained from the simulation of reheating by the FE code. The solutions of Eq.(2) and Eq.(3) by the FEM coupled model give the temperature distribution, strain rate and strain within the hot torsion sample.

Constitutive Equation and Deformation Conditions

A hyperbolic sine law, Eq. (5), modified by Hodgson and Collinson [19] was used to describe the flow stress of the steel under deformation conditions:

$$\bar{\sigma} = A_1 \bar{\varepsilon}^n \sinh^{-1}\left[A_2 \dot{\bar{\varepsilon}} \exp(\frac{Q}{RT}) \right]^m \qquad (5)$$

where Q is the deformation activation energy, R is the gas constant and T is the absolute temperature. Q, A_1, A_2, n and m are material constants. Identification of these parameters for the present steel can be found elsewhere [20].

The HTT specimens, with different gauge lengths and radii were designed in order to investigate the effect of specimen geometry on the distribution of thermo-mechanical parameters under various deformation conditions. It should be noted that the relationships between the sizes of the specimen, as shown in Figure 3a, were designed according to the basic stiffness requirement expressed in [10]. **Table 2** summarizes the dimensions of different specimens used in this study.

In all cases in the FE analysis, the angular velocity (ω) was chosen to be 1, 3 and 10 rad·s^{-1} and the temperature to be 1173, 1273 and 1373 K. Moreover, to generate identical effective strain ($\bar{\varepsilon} = 3$) the number of steps and time increment were calculated.

Table 2. Dimensional description of various HTT specimens (in mm)

Spec.	L1	R1	L2	R2	L3	R3	R4	L
G1	62	8	25	6.5	8	3.35	1	184
G2	62	8	12.5	5.5	33	3.35	1.5	184
G3	62	8	7	6.5	42	3.35	1.5	183
G4	62	8	3	6.5	52	3.35	1.5	185
G5	57	6.25	12.5	4.75	42	2.5	1.5	184
G6	66.5	9.25	3	8	41	4.25	2	184

Results and Discussion

Pre-deformation, reheating treatment. Figure 5 shows the calculated contour plots of the temperature distribution in various geometries of HTT specimens after applying the reheating cycle (Figure 1) and before starting deformation at 1273 K. It indicates that inductive heating may produce a non-uniform temperature along the axis of the specimens and could cause a temperature gradient within the gauge part of the specimen. As shown in Figure 5, specimens with a longer gauge are more susceptible to show a significant thermal gradient. For example in G4 (52mm gauge length), the temperature differential between centre
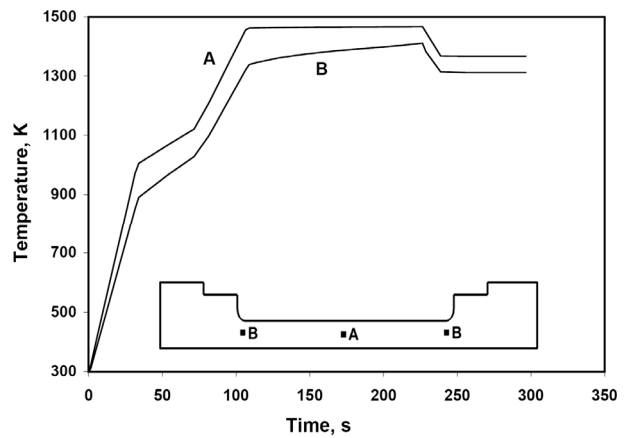

Figure 6. Temperature history at two points in the gauge section of G3 during reheating treatment.

and end of the gauge is the largest and about 433K. It should be noted that due to technical limitations, the induction coil length is fixed to 45mm for all specimens. This generates a two-dimensional heat flow, in radial and longitudinal directions of the gauge section, due to temperature difference between those sections of the specimen located inside and outside of the induction coil respectively. Consequently, the assumption of uniform temperature distribution in the gauge part of the specimen mentioned in previous works [10-13] may not be valid. This will have a negative impact on the final results of the test.

Variations of temperature during the reheating time for two points, A and B, in the gauge section of G3 during the reheating treatment are presented in **Figure 6**. It can be seen that the desired reheating cycle was only obtained at the centre of the specimen. The temperature at the ends of the gauge section deviates considerably from that specified by the programmed heating cycle. Consequently, a temperature of 1473 K that is needed for solution of the chemical elements could not be reached in these zones. Therefore, a homogeneous composition within the specimen could not be obtained before the start of deformation. Furthermore, different austenitizing temperatures at different points of the specimen lead to various austenite grain sizes, as discussed in [20].
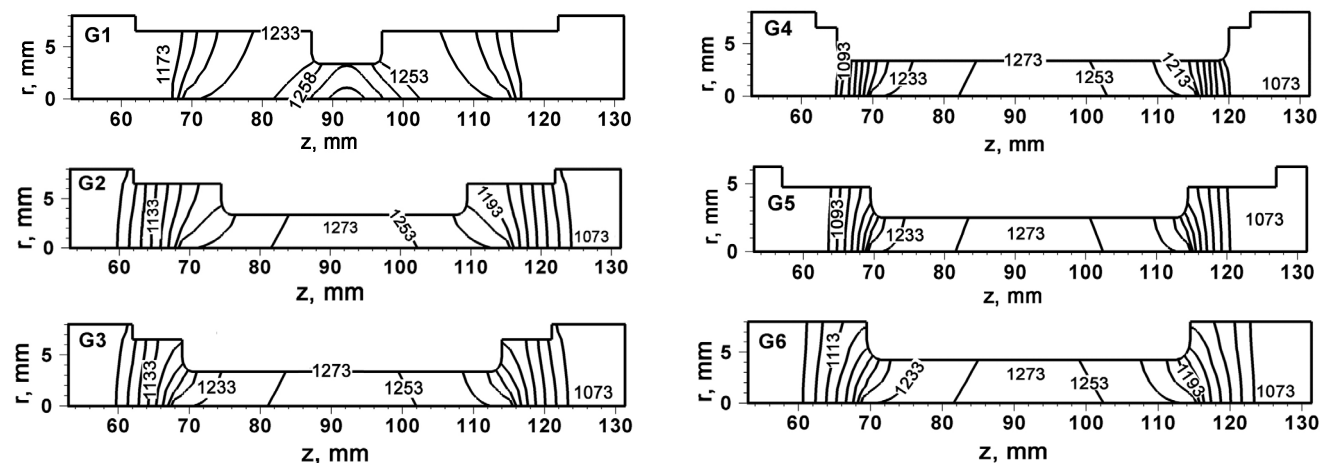

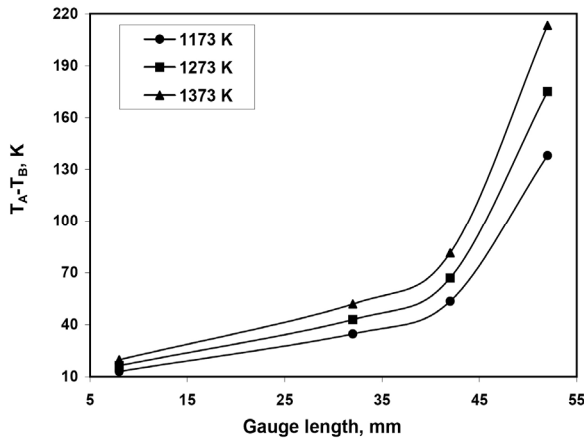**Figure 5.** Initial temperature (K) distribution in G1 - G6, after applying the reheating cycle.

Figure 7. Effect of gauge length on maximum differential temperature along the gauge section (induction coil of 45 mm length).
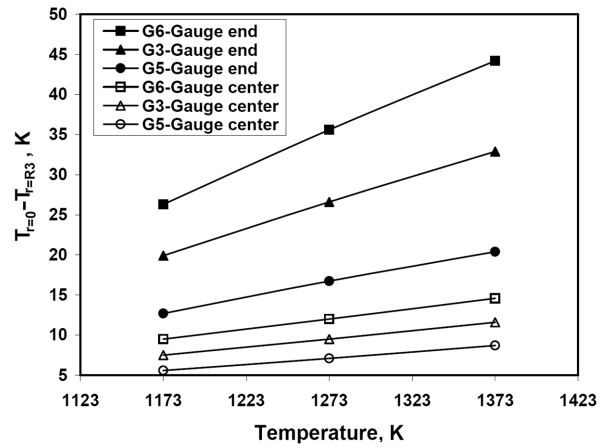

Figure 8. Temperature difference between the centre and the surface of the specimens after reheating and before the start of deformation at 1173, 1273 and 1373 K.

To evaluate the effect of gauge length on maximum temperature gradient along the gauge section, the value of temperature difference between points A and B (T_A- T_B) along the gauge section (Figure 6) was calculated for various specimens at different temperatures and plotted in **Figure 7**. This figure indicates that, as the gauge length increases, the value of (T_A- T_B) increases; so that for the specimen with 52 mm gauge length this gradient exceeds 473 K at 1373 K. It can also be observed that the initial temperature gradients prior to start of deformation at different temperatures are not similar. On the other hand, as the temperature decreases, the gradient decreases. It relates to the temperature difference between the gauge section and other parts of the specimen, which is less at lower temperatures than at higher temperatures. For a specimen with short gauge length, the results show that the initial temperature does not have much influence on the temperature gradient along the sample.

Figure 8 shows the temperature differential between the centre and the surface of the specimens in radial direction after reheating and holding and before the start of deformation at 1173, 1273 and 1373 K. As displayed in this figure, the radial variation of temperature is much less

than the temperature gradient in the axial direction. When the reheating treatment was finished at 1373 K, the maximum radial temperature gradient at both gauge centre and ends was greater compared to 1173 and 1273 K. However, at the middle of the specimen, the temperature difference between gauge surface and centre was less than 15 K.

The results presented show that for a given reheating cycle, the geometry of an HTT specimen has a great influence on the temperature distribution. So the assumption of constant temperature in the gauge section of the specimen in previous works [10-12, 14] can be unreliable and influence the interpretation of post-deformation results.

Choosing an inappropriate specimen geometry leads to a considerably non-uniform temperature distribution. Consequently, this causes a high non-homogeneous composition within the specimen and therefore any assessment of material properties during hot deformation could be unreliable. Among the investigated range of specimen geometries in this research, G1 and G2 specimens showed a low temperature gradient in both, longitudinal and radial directions of the gauge section. One may conclude that one criterion for the optimum geometry is to choose the sample length shorter than that of the induction coil.
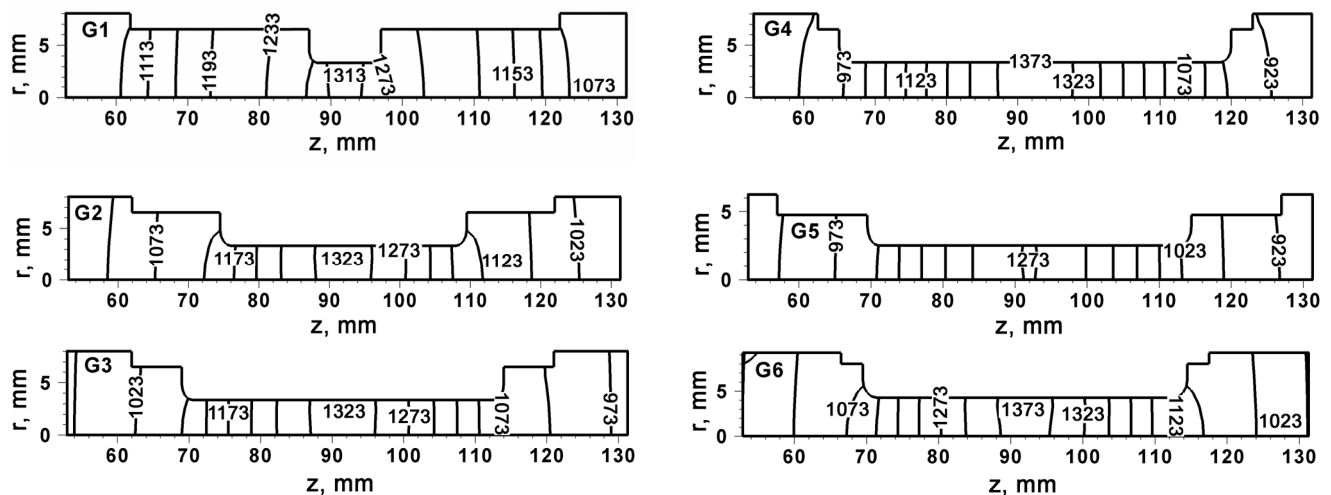

Figure 9. Temperature distribution in G1, G2, G3, G4, G5, and G6 deformed at 1273 K and ω = 3 rad·s^{-1}

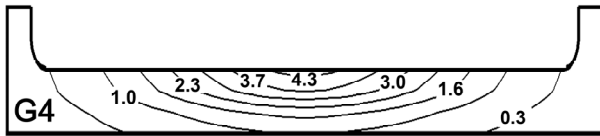Figure 10. Effective strain contour plot in G4 deformed at 1373 K and $\omega = 10$ rad·s^{-1}.

Figure 11. Flow localization in the specimen G4.

Post-deformation results. Figures 9 shows the contour plot of temperature distribution with different specimen geometries after deformation at 1273 K with a twist rate of $\omega = 3$ rad·s^{-1}. Comparing Figure 4 and Figure 9, one can see how temperature distribution has changed after deformation. In all specimens except G5 temperature increased at the centre of the gauge section because of heat generation due to the plastic deformation work. However, in specimens with 42mm and 52mm gauge length, temperature decreased at other points of the gauge section. It can be seen from the results that by increasing the gauge length, the thermal gradient along the specimen axis increases after deformation. This phenomenon can be explained by the long deformation time required for long specimens to reach required strain. During this time, considerable heat will be lost by different modes of heat transfer through the mini-shoulders, shoulders and the environment.

Comparison of the contour plots of temperature in G5, G3 and G6 (Figure) 9 indicates that increasing the gauge radius resulted in an increase of temperature at the gauge section. In fact, as the radius increased, the deformation rate increased. So for tick samples, much heat generation occurred and less time was provided for heat transfer.

Figure 10 shows the variations of strain contours for G4 deformed at 1373 K and $\omega = 10$ rad·s^{-1}. These may be explained by noting that for high twisting rates, the deformation time is very short and a high amount of heat is produced in the gauge section at the centre of the specimen. During deformation, this heat cannot be transferred fast enough to the interfacing shoulders and the environment. In addition, the ends of the gauge section in the long specimen, G4, are at lower temperature compared to the centre of the gauge section as seen in Figure 7. Consequently, due to a high temperature gradient in longitudinal direction and a considerable strain/strain rate change in the gauge section, flow localization will happen (**Figure 11**). This involves the mid gauge section experiencing softening phenomena, i.e. dynamic recrystallization, during deformation; while the ends of the gauge section cannot flow as easily as the centre. This results in flow localization. It could be concluded that long specimens deformed at high twisting rates are more susceptible to flow localization. In such cases, flow localization is unavoidable, and the obtained flow curve of the material includes a significant post processing error. Careful selection of the specimen geometry and twist rate leads to a minimum temperature gradient in the gauge section before and during the deformation and therefore, will minimize this problem. This might not be always achievable as for representing an industrial forming 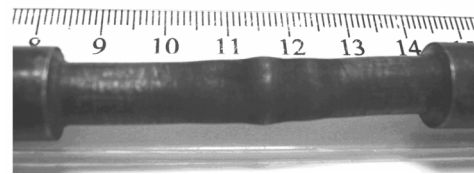process with a given strain rate, a given combination of the specimen geometry and twist rate is needed; these parameters do not necessarily match those of the optimized geometry and twist rate from the flow localization point of view. In order to reduce temperature variations in the gauge section of a long specimen, and consequently to minimize flow localization in the hot torsion test involving high strain rates, one may apply a non-uniform heat in the longitudinal direction. This, however, could have a negative impact on the distribution of the chemical composition within the materials.

The torque-twist angle curves of G1, G2, G3 and G4 specimens, deformed at a constant twist rate of $\omega = 3$ rad·s^{-1}, at initial temperatures of 1173, 1273 and 1373 K are shown in **Figure 12**. The results shown in **Figure 13** represent torque-twist calculated using G1, G2, G3 and G4 specimens at a fixed initial temperature of 1373 K, with different twist rates of $\omega = 1$, 3, 10 rad·s^{-1}. It shows the calculated rate sensitivity of the material at an initial temperature of 1373 K. The results shown in Figure 12 indicate that by reducing the deformation temperature, the flow curve is shifted upwards and the specimens show higher stiffness. This can also be seen from Eq.(5) where the flow stress is inversely proportional to the deformation temperature. The reduction of the torque is due to the easier movement of dislocations at higher temperatures, where more softening phenomena occur within the material. This in turn leads to the annihilation of dislocations at higher deformation temperatures. For rate sensitive materials, one expects that by increasing the twist rate at a constant temperature, a higher torque should be required to produce the same amount of deformation. This is not in agreement with the results shown in Figure 13; and could be explained by occurrence of flow localization at higher rates.

It can be seen in Figure 13 that at low strain rates, strain hardening behaviour is the dominant mechanism during deformation, while at high strain rates with a constant temperature perfectly plastic behaviour is more likely to happen. This is the case for G2, G3 and G4 specimens deformed at 1373 K and $\omega = 10$ rad·s^{-1}, where no significant strain hardening behaviour is observed. These are purely numerical results and the change of hardening trend is governed by the resultant of strain hardening nature of the constitutive equation used, hardening/ softening due to deformation heat and heat transfer during the deformation. A more realistic prediction requires incorporating mathematical models of dynamic recrystallization directly into the constitutive equation. Comparing Figures 12 and 13, one can see that for the cases investigated, the twist rate has a greater influence on flow stress than deformation temperature.
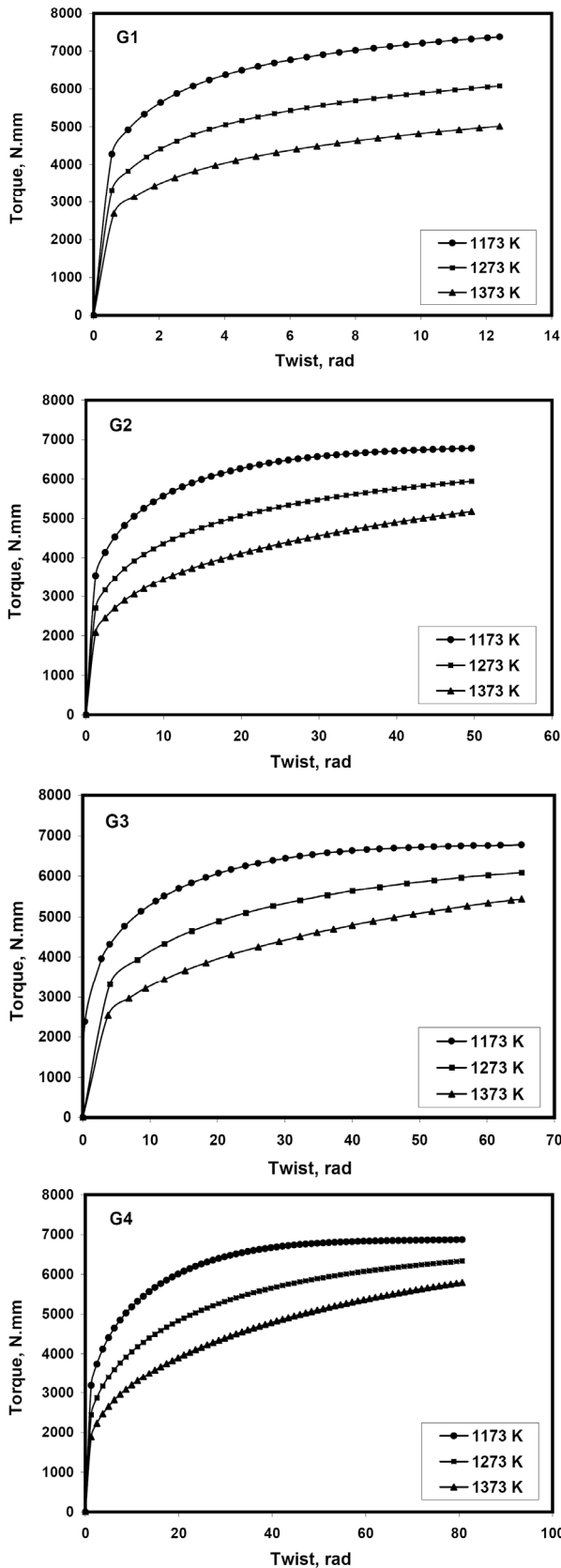
Figure 12. Torque-twist angle curves of G1 – G4 specimens deformed at ω = 3 rad·s^{-1} and 1173, 1273, 1373 K.

Figure 13. Torque-twist angle curves of G1 – G4 specimens deformed at 1373 K and ω = 1, 31 10 rad·s^{-1}.

The contour plots shown in **Figure 14a and 14b** display the calculated effective strains at the gauge section of G1 specimen assuming isothermal and non-isothermal conditions, r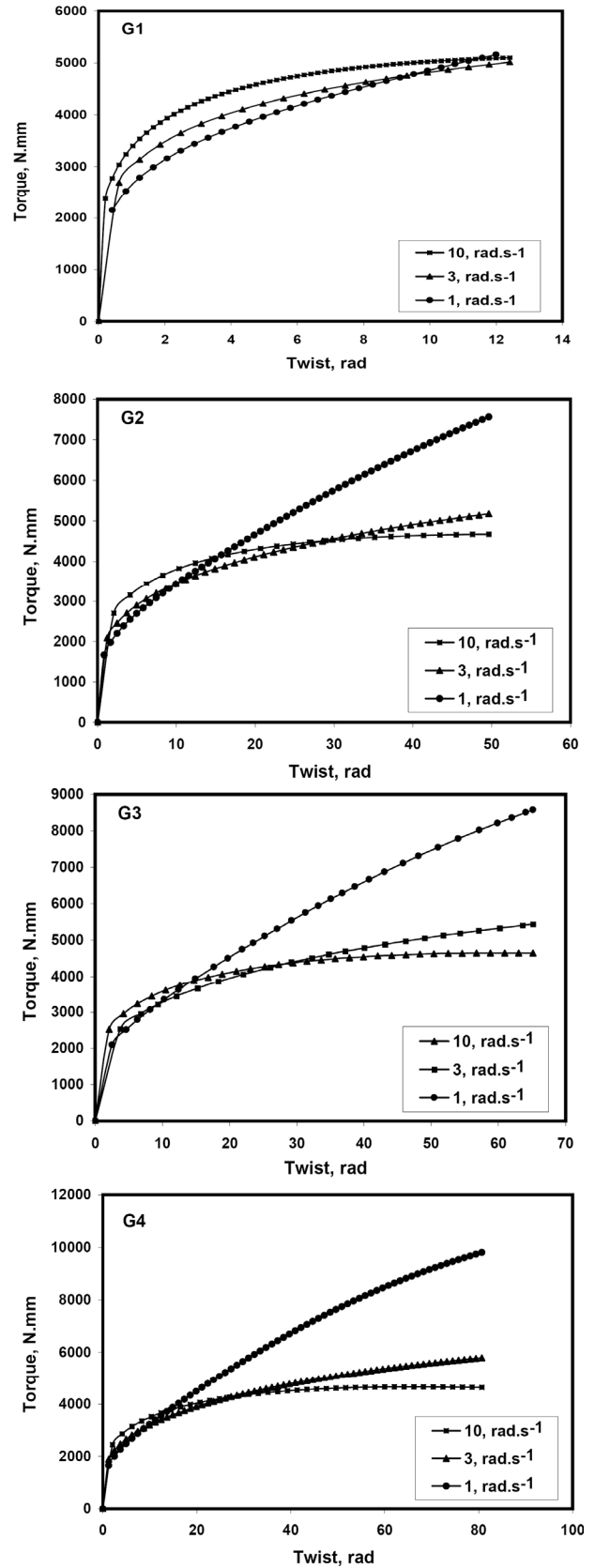espectively. It can be seen that for the isothermal assumption, no flow localization in the middle of the gauge section is predicted and the major deformation in the gauge section is a tubular pattern. **Figure 14c to 14e** show the calculated effective strains for the G2, G3 and G4
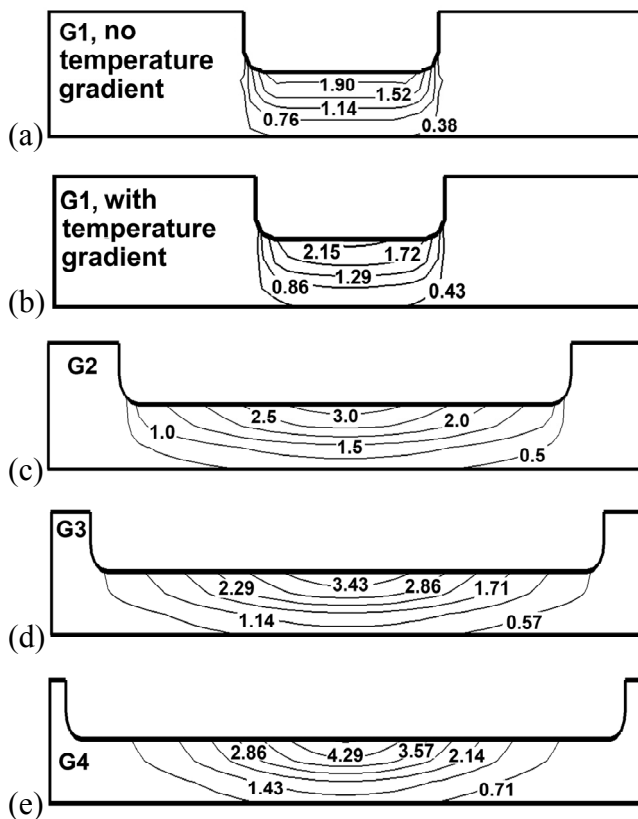
Figure 14. (a) and (b): Contour plots of effective strain of G1 with and without temperature gradient. (c) to (e): flow localization contour plots for G2, G3 and G4 deformed at ω = 3 rad·s⁻¹ and 1373 K.

specimens deformed at ω =3 rad·s⁻¹ and 1373 K which had a temperature gradient before starting deformation. The tests were originally designed to obtain an identical maximum effective strain ($\bar{\varepsilon} = 3$). In principle, for pure torsion with no temperature gradient, a tubular deformation pattern will develop and the strain at the constant radius remains the same along the gauge length. This is similar to the results shown in Figure 14a for G1 and isotherm deformation. The temperature gradient along the specimen's length changes the shape of the contour plot of effective strain. By increasing this gradient, not only the maximum strain accumulates at the centre of the gauge, but also the amount of strain increases at this point.

It is very difficult to judge the occurrence of flow localization without a computer aided design tool similar to the FE model presented in this paper. In the absence of a proper FE tool to design the test specimen, the extent of flow localization and therefore validity of the hot torsion test results at high strain rates could only be assessed by investigating the texture or hardness distribution in longitudinal and radial directions.

Conclusion and Summary

Comprehensive FE calculations were performed in this research to analyse the interaction of the geometry of hot torsion test specimens, reheating treatment and hot deformation conditions for API-X70 microalloyed steel by a coupled thermo-viscoplastic FE code. The results show that the specimens with a gauge length shorter than the induction coil length experience a low temperature gradient in both axial and radial directions after reheating. It is also shown that the longer specimens (G3 and G4) deformed at high twisting rates (10 rad·s⁻¹) were more susceptible to flow localization. Prevention of flow localization in these cases seems to be unachievable. Choosing an optimum geometry, however, may minimize this effect. Furthermore, strain contour plots indicate that a high temperature gradient results in accumulating strain at the centre of the sample, which could promote even more flow localization due to extra deformation heat.

The extent of flow localization depends on the temperature distribution before the start of deformation and the amount of heat generated during the deformation. The former is mostly dictated by the geometry of the test specimen and it also depends on the geometry and performance of the furnace. The latter is governed by the rate of deformation and is therefore more difficult to avoid. Generally speaking, for low twisting rates, a nearly steady state temperature distribution could be achieved. For higher deformation rates, however, it is not easy to establish a balance between heat gain and heat loss that occurs non-uniformly in the longitudinal/radial directions of the specimens. Therefore, such tests are more susceptible to flow localization. As a result, the results of high strain rate tests are less reliable. The scatter could be reduced if a method of local temperature control could be applied during the test. It must be noted, however, that any measurement of temperature and its distribution in the longitudinal and radial direction of the test specimen is very difficult. This makes the control of the temperature before and during the test a much more difficult task.

In the absence of proper instruments and technologies for measuring and controlling the temperature distribution in the test specimen, a computer aided tool, similar to the FE model presented in this article, is a must to validate the appropriateness of a test setup. The FE modelling presented in this article may be used to find a proper test specimen geometry and setup to minimize the effect of flow localization. This is especially true if the test is to be performed at high strain rates.

References

[1] F.H. Samuel, S. Yue, J.J. Jonas, B.A. Zbinden: ISIJ International, 29 (1989), No. 10, 878.
[2] D.Q Bia, S. Yue, W.P. Sun, J.J. Jonas: Metallurgical and Materials Transactions, 24A (1993), 2151.
[3] M. Carsi, V. Lopez, F. Penalba, O.A. Ruano: Materials Science and Engineering, A216 (1996), 155.
[4] P.D. Hodgson, L.X. Kong, C.H.J. Davies: Journal of Materials Processing Technology, 87 (1999), 131.
[5] A. Quispe, S.F. Medina: ISIJ International, 41 (2001), 174.

[6] D. Kuc, G. Niewielski, J. Cwajna: Materials Characterization, 56 (2006), 318.

[7] G. Dieter, A. Howard, S. Kuhn, L. Semiatin: Handbook of Workability and Process Design, ASM International, Materials Park, 2003.

[8] N. Rebelo, S. Kobayashi: International Journal of Mechanical Science, 22 (1980), 707.

[9] A. Moal, E. Massoni, J.L. Chenot: Computer Methods in Applied Mechanics and Engineering, 103 (1993), 434.

[10] S. Khoddam, Y.C. Lam, P.F. Thomson: Steel Research, 66 (1995), No. 2, 45.

[11] S. Khoddam: Thermo-mechanical rigid viscoplastic FE analysis of the hot torsion test for determining constitutive parameters, Ph.D. Thesis, Monash University, Australia (1997).

[12] M. Zhou, M.P. Clode: Computational Materials Science, 9 (1998), 411.

[13] R.K. Njiwa, G. Metauer, A. Marchal, J.V. Stebut: Journal of Materials Science, 36 (2001), 5659.

[14] S. Khoddama, P.D. Hodgson: Journal of Materials Processing Technology, 153-154 (2004), 839.

[15] User guide of OS550/OS550-BB series industrial infrared thermometer/transmitter, Appendix C: Determining an unknown emissivity, Omega, the USA, c-1.

[16] J. P. Holman: Heat Transfer, 9th ed., McGraw-Hill, Boston, 2002.

[17] S. Kobayashi, S.I. Oh, T. Altan: Metal Forming and the Finite Element Method, Oxford University Press, New York, 1989.

[18] F.L. Stasa: Applied Finite Element Analysis for Engineers, Holt, Rinehart and Winston, New York, 1985.

[19] P.D. Hodgson, D.C. Collinson: The calculation of hot strength in plate and strip rolling of niobium microalloyed steels, International Symposium on Mathematical Modeling of Hot Rolling of Steel, 1990, p. 239.

[20] B. Mirzakhani: Dynamic and static recrystallization behavior of microalloyed steel during thermomechanical process, M.Sc. Thesis, IUST, Tehran, Iran, 2002.

Detecting Large Inclusions in Steels: Evaluating Methods

Jens EKENGREN and Jens BERGSTRÖM

Department of Mechanical and Materials Engineering, Karlstad University, SE-651 88 Karlstad, Sweden. Jens.Ekengren@kau.se

The distribution of large non-metallic inclusions in two steel grades has been investigated using light optical microscopy, scanning electron microscopy and ultrasonic fatigue testing in the gigacycle range. The different methods have inherently different capabilities for finding inclusions in different size ranges. A measure of the distribution of large inclusions is proposed as the size S at which half of the fatigue specimens are expected to contain at least one inclusion of size S or larger. Values of S are obtained using the volume distribution estimated by the three methods. Extrapolation from microscopy measurements on surfaces agree with fatigue fractography results regarding density of large inclusions, as measured by the proposed ranking variable S.

Introdcution

Advanced high performance steels are an important group of materials, and obtaining accurate material data is vital for proper use. One important property is the fatigue strength at different cycle counts which is strongly connected to the densities of defects initiating failure, such as non-metallic inclusions. At large stress amplitudes and low fatigue life, any defect may act as a fatigue crack initiation point, but as the maximum stress level is decreased, the number of cycles to failure increases [1]. The decrease in allowable stress levels can be in the order of 20 %, ranging from 10^6 to 10^{10} cycles [2, 3].

The lower stress levels reduce the influence of small inclusions, as initiated cracks will be subcritical to the predicted life time. At extremely high cycle counts, i.e. in the Very High Cycle Fatigue (VHCF) regime, fatigue failure is usually initiated at inclusions or other internal defects [4–7].

The largest, and therefore the most detrimental, inclusions are very rare and it is not practical or even feasible to examine enough material to correctly assess the inclusion distribution below a certain occurrence probability [8]. In fatigue, it is assumed that failure generally occurs at the largest inclusion within the stressed volume [1].

This work is aimed at evaluating different inclusion detection methods with respect to their ability to predict the distribution of large inclusions in two steels. The methods used were surface area scanning methods using light optical microscopy according to Swedish Standard 11 11 16 [9] and scanning electron microscopy with automated inclusion detection software. Typical inclusion sizes for these methods and materials are in the range of about 2-3 μm to 25 μm. The area distribution thus obtained was converted to a volume distribution using a stereological method based on the Saltykov method. Also, two volume scanning methods were used, high frequency fatigue testing to 10^9 cycles and ultrasonic immersion tank measurements.

Testing

The methods used for detection of inclusions were ultrasonic fatigue testing to 10^9 cycles (gigacycle fatigue, GCF), ultrasonic immersion tank (UIT) measurements, light optical microscopy (LOM) and scanning electron microscopy with automated inclusion detection software (SEM).

Two high performance steels were examined in order to estimate the distribution of inclusions,